Electron-positron pair production in a bifrequent oscillating electric field

Ibrahim Akal,[1] Selym Villalba-Chávez,[1,*] and Carsten Müller[1]

[1] *Institut für Theoretische Physik I, Heinrich-Heine-Universität Düsseldorf, Universitätsstraße 1, 40225 Düsseldorf, Germany*

(Dated: December 9, 2014)

The production of electron-positron pairs from the quantum vacuum polarized by the superposition of a strong and a perturbative oscillating electric field mode is studied. Our outcomes rely on a nonequilibrium quantum field theoretical approach, described by the quantum kinetic Boltzmann-Vlasov equation. By superimposing the perturbative mode, the characteristic resonant effects and Rabi-like frequencies in the single-particle distribution function are modified, as compared to the predictions resulting from the case driven by a strong oscillating field mode only. This is demonstrated in the momentum spectra of the produced pairs. Moreover, the dependence of the total number of pairs on the intensity parameter of each mode is discussed and a strong enhancement found for large values of the relative Keldysh parameter.

PACS numbers: 12.20.-m, 11.10.Jj, 13.40.Em, 14.70.Bh.

arXiv:1409.1806v2 [hep-ph] 8 Dec 2014

I. INTRODUCTION

The spontaneous creation of electron-positron pairs in a strong external electric field is a remarkable nonperturbative phenomenon, intrinsically associated with the instability of the quantum vacuum [1–3]. In a constant electric field, this phenomenon–also known as the Schwinger mechanism–has a production rate exponentially small $\sim \exp(-\pi E_c/E)$. Hence, its occurrence is expected to be difficult to achieve experimentally, unless the electric field strength E comes close to the critical scale of quantum electrodynamics (QED) $E_c = 1.3 \times 10^{16}$ V/cm. Unfortunately, a field of such a nature is not within the reach of current technical capabilities and a direct experimental observation of the Schwinger mechanism remains a big challenge for the contemporary physics. Hopes of reaching the required field strengths in the focal spot of envisaged high-intensity lasers such as the Extreme Light Infrastructure (ELI) [4] and the Exawatt Center for Extreme Light Studies (XCELS) [5] have renewed the interest in the study of Schwinger-like pair production (PP) processes. Its verification will provide significant insights in the nonlinear QED regime as well as in various processes which share its nonperturbative feature. Notably, among them are the Unruh and Hawking radiation and the string breaking in the theory of the strong interactions [6].

While the prospect of using the strong field of lasers is enticing from practical perspectives, there exists a price to be paid for: the complicated nature of the electromagnetic field of a laser pulse–the wave profile, its spacetime dependence and the existence of magnetic field components–introduces considerable additional complications in the calculations associated with the PP process. Indeed, it seems that a full description of the vacuum decay in such a scenario is far from being computationally feasible, at least in the near future. In order to make the problem tractable some simplifications are required.[1] In the first instance, an analysis in a pure electric field would be highly desirable since, on the one hand, it resembles the electric-like background used in the genuine Schwinger mechanism, and on the other hand because this special field configuration can be obtained to a good approximation through a collision of two counterpropagating linearly polarized laser pulses with equal intensities and polarization directions. The resulting field is a standing electromagnetic wave depending separately upon the spatial and temporal coordinates. This setup substantially simplifies the treatment of the problem, but the field inhomogenity still represents a major task to overcome from analytic and numeric viewpoints. Although some progresses in the latter direction have been accomplished already [9–13], most of the theoretical efforts carried out so far have been focused on the idealization in which the background is a homogeneous electric field oscillating in time [14, 15]. As such, this temporal dependence renders the vacuum decay into electron-positron pairs a far from equilibrium phenomenon. Consequently, the quantum kinetic theory has turned out to be an appropriate formalism for analyzing the aforementioned process [16–18].

In parallel, various mechanisms for compensating the suppression associated with the spontaneous creation of electron-positron pairs from the vacuum have been put forward [19–30]. Some of them have been motivated by the fact that pair production by multiphoton absorption has been observed using nonlinear Compton scattering [31]. In line with this issue, the authors of Refs. [19, 20] showed that the pair creation rate can be enhanced by

*Electronic address: selym@tp1.uni-duesseldorf.de

[1] Obviously, the plane-wave approximation is excluded, because in this case the field invariants $\mathscr{F} = (E^2 - B^2)/2$ and $\mathscr{G} = \boldsymbol{E} \cdot \boldsymbol{B}$ vanish identically, and the vacuum-vacuum transition amplitude does not decay against electron-positron pairs [7, 8].

superimposing a weak beam of energetic photons with a strong but low-frequency electric field. The study of such a problem was carried out by taking the slow laser pulse as a constant electric field reducing the problem to that of a photon-stimulated Schwinger pair creation. The idea has been further extended to the case in which both pulses are Sauter fields with different time scales [32, 33]. However, in more realistic setups it is expected that the subcycle structure of an oscillating electric field (OEF) plays a relevant role as it provides a phenomenology characterized by resonant effects and Rabi-like oscillations [34–39]. To the best of our knowledge, the study of such a problem in a bifrequent OEF composed of a strong and a weak mode has not been addressed so far. Hence, we aim to show how these features are manifest in the dynamical-assisted Schwinger mechanism and reveal their consequences in the total density of produced pairs. For other recent studies of pair production processes in bifrequent electromagnetic fields, we refer the interested reader to Refs. [40, 41].

Apart from this introductory portion, our paper has three additional sections. In Sec. II we describe some basic features of the PP process within the framework of the quantum Boltzmann-Vlasov equation. Afterwards, its solution in a periodic multimode OEF is derived and a study of the resonant effects and Rabi-like oscillations is carried out. The numerical results are exposed in Sec. III for the particular situation in which a two-mode OEF is considered. There, different issues associated with the production mechanism for various frequency combinations are discussed. Special attention is paid to the effects caused by the superposition of a strong and perturbative mode on the single-particle distribution function. The density of pairs yielded in such a configuration is also investigated. Further comments and remarks are finally given in the Conclusion.

II. QUANTUM KINETIC APPROACH

A. The quantum Boltzmann-Vlasov equation

We consider the production of electron-positron pairs from a vacuum polarized by an external classical electromagnetic field which is described by a spatially homogeneous but time-dependent four-potential $\mathcal{A}_\mu(t)$. With the former assumption we are implicitly disregarding the potential realization of avalanche processes [42] that could dim the field strength. The latter condition implies that the field can be Fourier-expanded in terms of the canonical momentum $\boldsymbol{p}$ and, additionally, prevents the existence of magnetic field components. Note that, according to Noether's theorem, the total momentum of each created pair will always sum up to zero. Thus, the creation of an electron with momentum $\boldsymbol{p}$ is always accompanied by the creation of a positron with momentum $-\boldsymbol{p}$ in the purely time-dependent external field.

For further convenience, we will choose $\mathcal{A}_\mu(t)$ fulfilling the temporal gauge–i.e., $\mathcal{A}_0(t) = 0$–so that the nonvanishing electric field is given by $\boldsymbol{E}(t) = -d\boldsymbol{\mathcal{A}}/dt = (0, E(t), 0)$ pointing in the y direction. Hereafter, we focus ourselves in the subcritical regime $E \ll E_c = m^2/|e|$, where m and e are the electron mass and charge, respectively.[2] Also, in what follows, we take into account neither the collision between the created particles nor their inherent radiation fields. Previous investigations on these subjects have revealed that the effects induced by both phenomena are irrelevant for the PP whenever the field strength E is weaker than the critical one E_c [43–45] and this is in fact the regime in which we are interested.

We note that only those Lorentz transformations which leave the external field invariant describe the formal invariance properties of the vacuum in the presence of the field.[3] Since they form a subgroup of the full Lorentz symmetry group and the concept of one-particle states relies on the irreducible representations of the latter group [49], one finds that the standard classification of elementary particles is no longer applicable in the region occupied by an external field. Despite this conceptual loss, the canonical quantization of the matter sector of QED in an OEF can be carried out [7]. A relevant step in this direction results from the diagonalization of the corresponding Hamiltonian in every instant of time through time-dependent Bogolyubov transformations. Such a procedure allows us to express the spinor field operator in terms of degrees of freedom in the external field, i. e., in the so-called quasiparticles representation:

$$\begin{aligned} \Psi(\boldsymbol{x},t) &= \frac{1}{L^{3/2}}\sum_{\boldsymbol{p}} \Phi_{\boldsymbol{p}}(t) e^{i\boldsymbol{p}\cdot\boldsymbol{x}}, \\ \Phi_{\boldsymbol{p}}(t) &= \sum_{s} \left\{ a_{\boldsymbol{p},s}(t) u_{\boldsymbol{p},s}(t) + b^{\dagger}_{-\boldsymbol{p},s}(t) v_{-\boldsymbol{p},s}(t) \right\}, \end{aligned} \tag{1}$$

where $V = L^3$ is the normalization volume and $\boldsymbol{p} = \frac{2\pi}{L}\boldsymbol{n}$ the discretized momentum with $\boldsymbol{n} = (n_x, n_y, n_z)$, $n_i = 0, \pm 1, \pm 2, \ldots$ In this framework, the time-dependent bispinors $u_{\boldsymbol{p},s}(t)$ and $v_{\boldsymbol{p},s}(t)$ are eigenfunctions of the boost operator component along the external field direction with eigenvalues $s = \pm 1/2$. While $a_{\boldsymbol{p},s}(t)$ and $a^{\dagger}_{\boldsymbol{p},s}(t)$ represent the corresponding annihilation and creation operators for a quasiparticle, $b^{\dagger}_{-\boldsymbol{p},s}(t)$ and $b_{-\boldsymbol{p},s}(t)$ are the creation and annihilation operators for an antiquasiparticle, respectively. These two sets of instantaneous second quantization operators satisfy the equal time anticommu-

[2] Here and henceforth we use natural units in which the speed of light c and the Planck constant $\hbar$ are equal to unity, $c = \hbar = 1$.

[3] This statement is in line with previous group-theoretical analyses developed in an external constant electromagnetic field [46, 47] and in the case in which the background is a circularly polarized plane wave [48].

tation relations

$$\left[a_{\boldsymbol{p},s}(t), a^{\dagger}_{\boldsymbol{p}',s'}(t)\right]_{+} = \delta_{\boldsymbol{p},\boldsymbol{p}'}\delta_{s,s'}, \tag{2}$$

$$\left[b_{\boldsymbol{p},s}(t), b^{\dagger}_{\boldsymbol{p}',s'}(t)\right]_{+} = \delta_{\boldsymbol{p},\boldsymbol{p}'}\delta_{s,s'}, \tag{3}$$

and all other anticommutators vanish identically. Because of their temporal dependences, one can introduce quantities that arise naturally in the study of transport phenomena such as the single-particle distribution function

$$W(\boldsymbol{p},t) = \sum_{s}\langle \mathrm{VAC,in}|a^{\dagger}_{\boldsymbol{p},s}(t)a_{\boldsymbol{p},s}(t)|\mathrm{VAC,in}\rangle \tag{4}$$

where the ground state $|\mathrm{VAC,in}\rangle$ is defined in the Heisenberg picture by $a_{\mathrm{in}}|\mathrm{VAC,in}\rangle = b_{\mathrm{in}}|\mathrm{VAC,in}\rangle = 0$ with $a_{\mathrm{in}} \equiv a_{\boldsymbol{p},s}$ and $b_{\mathrm{in}} \equiv b_{-\boldsymbol{p},s}$ at $t \to t_{\mathrm{in}}$. The connection between the in-operators and the instantaneous ones involved in Eqs. (2) and (3) is mediated by certain Bogolyubov coefficients $f(\boldsymbol{p},t)$ and $g(\boldsymbol{p},t)$ [see details in Appendix A]. As a consequence, the time evolution equations of $W(\boldsymbol{p},t) = 2|f(\boldsymbol{p},t)|^2$ follow from the temporal equations of $f(\boldsymbol{p},t)$. The latter can be determined by exploiting the fact that the field representations [Eq. (1)] satisfy the Dirac equation in the external field. This procedure leads to a system of coupled ordinary differential equations (ODEs) that have been extensively exploited in the study of several open questions associated with the PP process [32, 35, 39, 50, 51]. In particular, by following the notation of Ref. [39], it reads

$$i\dot{f}(\boldsymbol{p},t) = \mathcal{a}_{\boldsymbol{p}}(t)f(\boldsymbol{p},t) + \mathcal{b}_{\boldsymbol{p}}(t)g(\boldsymbol{p},t), \tag{5}$$

$$i\dot{g}(\boldsymbol{p},t) = \mathcal{b}^{*}_{\boldsymbol{p}}(t)f(\boldsymbol{p},t) - \mathcal{a}_{\boldsymbol{p}}(t)g(\boldsymbol{p},t) \tag{6}$$

with the initial conditions $f(\boldsymbol{p},-\infty) = 0$ and $g(\boldsymbol{p},-\infty) = 1$. Note that, hereafter, a dot indicates a total time derivative. The remaining functions and parameters contained in these formulas are given by

$$\mathcal{a}_{\boldsymbol{p}}(t) = \mathcal{w}_{\boldsymbol{p}}(t) + \frac{eE(t)p_x}{2\mathcal{w}_{\boldsymbol{p}}(t)(\mathcal{w}_{\boldsymbol{p}}(t)+m)}, \tag{7}$$

$$\mathcal{b}_{\boldsymbol{p}}(t) = \frac{1}{2}\frac{eE(t)\epsilon_{\perp}}{\mathcal{w}^2_{\boldsymbol{p}}(t)}\exp\left[-i\arctan\left(\frac{p_x q_{\parallel}}{\epsilon^2_{\perp}+\mathcal{w}_{\boldsymbol{p}}(t)m}\right)\right], \tag{8}$$

where the kinetic momentum along $\boldsymbol{E}$ is defined as $q_{\parallel}(t) = p_{\parallel} - e\mathcal{A}(t)$. In this context, $\epsilon^2_{\perp} = m^2 + \boldsymbol{p}^2_{\perp}$ is the transverse energy squared, whereas $\mathcal{w}^2_{\boldsymbol{p}}(t) = \epsilon^2_{\perp} + q^2_{\parallel}(t)$ characterizes the total energy squared. Here $\boldsymbol{p}_{\perp} = (p_x, 0, p_z)$ with $p_z = 0$ and $\boldsymbol{p}_{\parallel} = (0, p_y, 0)$ are the components of the canonical momentum perpendicular and parallel to the direction of the field, respectively. We emphasize that, due to the cylindrical symmetry of the problem about the y axis, we may set $p_z = 0$ without loss of generality.

Although Eqs. (5) and (6)–with Eqs. (7) and (8) included–turn out to be appropriate for a numerical assessment, there exists an integrodifferential equation for $W(\boldsymbol{p},t)$ which allows us to extract some important outcomes from the PP process:

$$\begin{aligned}\dot{W}(\boldsymbol{p},t) &= \partial_t W(\boldsymbol{p},t) + eE(t)\partial_{q_{\parallel}}W(\boldsymbol{p},t) \\ &= \frac{eE(t)\epsilon_{\perp}}{\mathcal{w}^2_{\boldsymbol{p}}(t)}\int_{-\infty}^{t}dt'\frac{eE(t')\epsilon_{\perp}}{\mathcal{w}^2_{\boldsymbol{p}}(t')}[1-W(\boldsymbol{p},t')] \\ &\times\cos\left[2\int_{t'}^{t}dt''\ \mathcal{w}_{\boldsymbol{p}}(t'')\right].\end{aligned} \tag{9}$$

The above formula–also known as the quantum Boltzmann-Vlasov equation–assumes the vacuum initial condition $W(\boldsymbol{p},-\infty) = 0$. Its derivation from Eqs. (5) and (6) is outlined in Appendix B.

Eq. (9) shows that the PP is a nonequilibrium time-dependent process. Besides, it has been recognized that the combination of the nonlocality in time and the memory effects closely associated with the quantum statistic factor $\sim 1 - W(\boldsymbol{p},t)$ provides Eq. (9) with a pronounced non-Markovian feature [16, 44, 50]. It means that the single-particle distribution function depends on the number of degrees of freedom already present in the system. We should also mention at this point that the experimentally observable fields are those resulting at asymptotically large times [$t \to \pm\infty$], when the electric field is switched off $\boldsymbol{E}(\pm\infty) \to 0$. These are the electron and positron one-particle states to which the degrees of freedom in an OEF are relaxed at this asymptotic condition. Accordingly, the asymptotic single-particle distribution function $W(\boldsymbol{p},\infty)$ is physically meaningful.[4]

Finally, we wish to stress that the integration over the momentum, i. e.,

$$\mathcal{N}_{e^-e^+} = \lim_{t\to\infty}\int \mathrm{đ}^3p\, W(\boldsymbol{p},t) \tag{10}$$

defines the number of produced pairs per unit of volume. Observe that the shorthand notation $\mathrm{đ} = d/(2\pi)$ has been used here. It is worth observing that the corresponding particle creation rate differs from the asymptotic expression of the vacuum decay rate per unit of volume $\Gamma_{\mathrm{vac}}(t)$ given in Eq. (A12). Only when the condition $|f(\boldsymbol{p},\infty)|^2 \ll 1$ is fulfilled one can approach $\Gamma_{\mathrm{vac}}(\infty) \approx -\dot{\mathcal{N}}_{e^-e^+}$. However, we will see very shortly that–owing to resonant effects–the former limit is not always satisfied in an OEF, requiring a clear distinction between both concepts.

B. Resonance effects and Rabi-like oscillations in a multimode standing electric wave

The PP in an OEF is characterized by resonance effects associated with the absorption of multiple energy pack-

[4] How far the physical interpretation of quasiparticle states in the presence of an external field can be stretched has recently been addressed in Ref. [52].

ages ["photons"] from the external field and by Rabi-like oscillations. This result has been found by Popov [34] and further developed by other authors [37–39, 53] for a single-mode OEF. In this subsection, we show how both properties are manifest in the presence of a multimode OEF and within the framework of nonequilibrium quantum field theory. To this end, we will study an equivalent representation of Eq. (9) [see details in Appendix B]:

$$\dot{\bar{f}}(\boldsymbol{p},t) = -\frac{eE(t)\epsilon_\perp}{2\varpi^2_{\boldsymbol{p}}(t)}\bar{g}(\boldsymbol{p},t)\exp\left[2i\int_{t_0}^{t} dt'\ \varpi_{\boldsymbol{p}}(t')\right], \quad (11)$$

$$\dot{\bar{g}}(\boldsymbol{p},t) = \frac{eE(t)\epsilon_\perp}{2\varpi^2_{\boldsymbol{p}}(t)}\bar{f}(\boldsymbol{p},t)\exp\left[-2i\int_{t_0}^{t} dt'\ \varpi_{\boldsymbol{p}}(t')\right], \quad (12)$$

in which the lower integration limit t_0 sets an arbitrary phase at a given instant of time and $W(\boldsymbol{p},t) = 2|\bar{f}(\boldsymbol{p},t)|^2$. Next, we decompose the vector potential comprising k modes according to

$$\mathcal{A}_\mu(\eta_1,\ldots,\eta_k) = \sum_{i=1}^{k}\mathcal{A}^{(i)}_\mu(\eta_i), \quad \text{with} \quad \eta_i = \omega_i t. \quad (13)$$

Each mode $\mathcal{A}^{(i)}_\mu(\eta_i)$ is supposed to be a $2\pi-$periodic function in the variable η_i. The resulting field $\mathcal{A}_\mu(\eta_1,\ldots,\eta_k)$ does not have a well-defined periodicity in time. However, it turns out to be a periodic function in each variable $\eta_1,\ \eta_2,\ldots,\ \eta_k$ separately. By taking advantage of this fact, a periodic part $\tilde{\Theta}_{\boldsymbol{p}}(\eta_1,\ldots,\eta_k)$ can be separated in the dynamical phase $\int_{t_0}^{t} dt'\ \varpi_{\boldsymbol{p}}(t') = \bar{\varepsilon}_{\boldsymbol{p}}t + \tilde{\Theta}_{\boldsymbol{p}}(\eta_1,\ldots,\eta_k)$, with $\bar{\varepsilon}_{\boldsymbol{p}}$ being the electron quasienergy. In correspondence, we expand the product of functions contained in Eqs. (11) and (12) in Fourier series:

$$\frac{eE(t)\epsilon_\perp}{\varpi^2_{\boldsymbol{p}}(t)}\exp\left[2i\int_{t_0}^{t} dt'\ \varpi_{\boldsymbol{p}}(t')\right] \simeq \sum_{n_1\ldots n_k=-\infty}^{\infty}\Lambda_{n_1,\ldots,n_k}(\boldsymbol{p}) \times\exp\left[2i\bar{\varepsilon}_{\boldsymbol{p}}t - i\sum_{j=1}^{k} n_j\eta_j\right]. \quad (14)$$

Here the Fourier coefficients are k-fold parametric integrals given by

$$\Lambda_{n_1,\ldots,n_k}(\boldsymbol{p}) = \int_{-\pi}^{\pi}\text{đ}\eta_1\ldots\int_{-\pi}^{\pi}\text{đ}\eta_k\frac{eE(\eta_1,\ldots,\eta_k)\epsilon_\perp}{\varpi^2_{\boldsymbol{p}}(\eta_1,\ldots,\eta_k)} \times\exp\left[2i\tilde{\Theta}_{\boldsymbol{p}}(\eta_1,\ldots,\eta_k) + i\sum_{j=1}^{k} n_j\eta_j\right] \quad (15)$$

whose explicit expression is not important to show the generic nature of the process.

Note that the only place where the time enters in Eq. (14) is in the exponentials. Because of this, they will oscillate wildly as the limit $t\to\pm\infty$ is taken into account. As such, the combination which minimizes the exponent is dominant and promotes the energy conservation in the PP processes

$$2\bar{\varepsilon}_{\boldsymbol{p}} = \sum_{j=1}^{k} n_j\omega_j. \quad (16)$$

The corresponding Fourier indices are denoted by $n_1,\ldots,n_k$ here. When fast-varying terms are dropped, Eq. (14) can be approached by its most slowly varying Fourier mode[5]

$$\frac{eE(t)\epsilon_\perp}{\varpi^2_{\boldsymbol{p}}(t)}\exp\left[2i\int_{t_0}^{t} dt'\ \varpi_{\boldsymbol{p}}(t')\right] \approx \Lambda_{n_1,\ldots,n_k}(\boldsymbol{p}) \times\exp\left[i\Delta_{n_1,\ldots,n_k}(\boldsymbol{p})t\right] \quad (17)$$

with $\Delta_{n_1,\ldots,n_k}(\boldsymbol{p}) \equiv 2\bar{\varepsilon}_{\boldsymbol{p}} - \sum_j n_j\omega_j$ being the detuning parameter. Owing to this approximation, Eqs. (11) and (12) reduce to an ODE system whose solutions can be found without too much effort. Indeed, the resulting $\bar{f}(\boldsymbol{p},t)$ allows us to express the single-particle distribution function as

$$W_{n_1,\ldots,n_k}(\boldsymbol{p},t) \approx \frac{1}{2}\frac{|\Lambda_{n_1,\ldots,n_k}(\boldsymbol{p})|^2}{\Omega^2_{\text{Rabi}}(\boldsymbol{p})} \times\sin^2\left[\Omega_{\text{Rabi}}(\boldsymbol{p})(t-t_{\text{in}})\right],$$

where we have supposed that the field is suddenly turned on at t_{in} with $\bar{f}(\boldsymbol{p},t_{\text{in}}) = 0$ and $\bar{g}(\boldsymbol{p},t_{\text{in}}) = 1$. Here the Rabi-like frequency of the vacuum is given by

$$\Omega_{\text{Rabi}}(\boldsymbol{p}) \equiv \frac{1}{2}\left[|\Lambda_{n_1,\ldots,n_k}(\boldsymbol{p})|^2 + \Delta^2_{n_1,\ldots,n_k}(\boldsymbol{p})\right]^{1/2}. \quad (18)$$

That the single-particle distribution function oscillates with this frequency is a clear manifestation of the vacuum instability in a multimode OEF. This statement can be verified by supposing that the standing wave is instantaneously turned off after the interaction time $\tau = t_{\text{out}} - t_{\text{in}}$. For simplicity we set the momenta to zero $\boldsymbol{p} = 0$ and study Eq. (18) near resonance $\Delta_{n_1,\ldots,n_k} \simeq 0$.[6] In such a case, the Rabi-like frequency of the vacuum approaches $\Omega^{(0)}_{\text{Rabi}} \equiv \Omega_{\text{Rabi}}(0) \approx \frac{1}{2}|\Lambda_{n_1,\ldots,n_k}(0)|$ and the distribution function acquires the form

$$W_{n_1,\ldots,n_k}(t) \approx \begin{cases} 2\sin^2\left[\Omega^{(0)}_{\text{Rabi}}(t-t_{\text{in}})\right], & t < t_{\text{out}} \\ 2\sin^2\left[\Omega^{(0)}_{\text{Rabi}}\tau\right], & t \geqslant t_{\text{out}} \end{cases}. \quad (19)$$

The above formula shows an oscillatory pattern resulting from continuous transitions characterized by a period $\mathcal{T} = 2\pi/\Omega^{(0)}_{\text{Rabi}}$. This effect resembles the Rabi oscillation associated with a driven two-level atomic system. In accordance, Eq. (19) provides an evidence that in the field of a multimode OEF, the number of quasiparticles in a vanishing momentum state is not stationary. Clearly, for

[5] For commensurable field frequencies $\omega_1,\ldots,\omega_k$, there can be more than one exact solution of Eq. (16). Also, in the incommensurable case, several integer combinations of frequencies may solve Eq. (16) approximately (see Sec.III-C). Hence, in general, there can be more than just one dominant Fourier mode.

[6] Away from the resonance, the oscillations are faster, but their amplitude is lower.

times larger than the interaction time [$t > \tau$], the distribution function for the asymptotic states is constant in time, which indicates that both the quantum vacuum and the created electron-positron pairs reach the required stability to carry out experimental measurements.

III. NUMERICAL ASPECTS AND RESULTS

In this section we perform a detailed numerical analysis of the PP process in a bifrequent oscillating electric field (bOEF). To this end, we have implemented a C++ code capable of solving the system of coupled ODEs given in Eqs. (5) and (6). Our goal is to investigate the assisted Schwinger mechanism resulting from the combination of a strong and a perturbative field mode. To make a clear distinction between these two different modes it is convenient to introduce the dimensionless intensity parameters

$$\xi_j = \frac{eE_j}{m\omega_j} \quad \text{with} \quad j \in \{1,2\}. \tag{20}$$

Here ω_j and E_j are the frequency and the electric field amplitude, respectively, of the jth mode. For the strong mode, we shall set the field attributes to $\xi_1 = 1.0$ and $\omega_1 = 0.3m$, which leads to a field strength of $E_1 = 0.3E_c$. In contrast, for the perturbative mode, we shall apply $\xi_2 \ll 1$ and a variable frequency ω_2.

Let us put the chosen field parameters into perspective. Today, a strong wave with the described characteristics is beyond the reach of the existing laser technology, even for the ELI and XCELS projects [4], where $E \lesssim 10^{-2}E_c$ in the optical regime $\omega \sim 1$ eV is envisaged corresponding to $\xi \lesssim 10^3$. Substantially higher photon energies of the order of $\omega \lesssim 10$ keV are available at modern x-ray free-electron laser facilities such as the Linac Coherent Light Source at SLAC (Stanford, California). But the maximum field strengths there lie 3 to 4 orders of magnitude below E_c, corresponding to $\xi \lesssim 10^{-2}$ (see Sec. II. in Ref. [54] and references therein). The motivation for our choice of parameters is, on the one hand, to allow for better insights into the PP process in a boEF by highlighting its intrinsic phenomenology and, on the other hand, to render the numerical computations feasible.

In order to avoid numerical inaccuracies at starting and ending points of the bOEF, we choose a modulated linear polarized potential of the form

$$\begin{aligned}\boldsymbol{\mathcal{A}}(\eta_1) = &-\frac{m\xi_1}{e}\sin(\eta_1)F_1(\eta_1)\hat{\boldsymbol{y}} \\ &-\frac{m\xi_2}{e}\sin(\Delta\omega\eta_1)F_2(\eta_1)\hat{\boldsymbol{y}},\end{aligned} \tag{21}$$

where $\eta_1 = \omega_1 t$, $\Delta\omega = \omega_2/\omega_1$ and $\hat{\boldsymbol{y}} = (0,1,0)^T$ defines the polarization direction of the field. In Eq. (21) the envelope functions $F_1(\eta_1)$ and $F_2(\eta_1)$ generally allow us to construct a field of any specific time duration separately for both modes. In the present study, however, we shall assume a uniform envelope function $F_1(\eta) = F_2(\eta) \equiv F(\eta)$, with $\sin^2$-shaped turn-on and turn-off segments and a plateau region of constant field intensity in between. It is given by

$$F(\eta) = \begin{cases} \sin^2\left(\frac{\eta}{4\delta_{\text{onoff}}}\right) & 0 \leqslant \eta < 2\pi\delta_{\text{onoff}} \\ 1 & 2\pi\delta_{\text{onoff}} \leqslant \eta \leqslant 2\pi K \\ \sin^2\left(\frac{N\pi}{2\delta_{\text{onoff}}} - \frac{\eta}{4\delta_{\text{onoff}}}\right) & 2\pi K < \eta \leqslant 2\pi N \\ 0 & \text{otherwise} \end{cases}, \tag{22}$$

where $N = N_{\text{plateau}} + 2\delta_{\text{onoff}}$ and $K = N - \delta_{\text{onoff}}$ hold. The lengths of the turn-on and turn-off segments of the field will be chosen throughout as $\delta_{\text{onoff}} = 0.5$. The plateau region comprises N_{plateau} field cycles. Consequently, the resulting total time duration of the bOEF is given by $N = N_{\text{plateau}} + 1$ in units of the strong mode period $\tau_{\text{cycle}} = 2\pi/\omega_1$.

Notice, that Eq. (21) with Eq. (22) included guarantees the starting of the bOEF with zero amplitude at $t = 0$. Besides, in order to improve the stability of the numerical integration scheme, all computations have been started half a period earlier than $t = 0$ when there is no field present. Similarly, all computations have been ended half a period after the external field has been switched off.

A. Resonance spectrum

We start our analysis by studying the dependence of the single-particle distribution function on the frequency of the weak mode. To this end, the latter has been varied within the interval $0.2m \leq \omega_2 \leq 2.5m$. Here, we first consider the case that the particles are created with zero momentum ($\boldsymbol{p} = 0$). The particles' momentum spectra will be discussed in Sec.III.C below.

For a given value of ω_2, the number of plateau cycles N_{plateau} has been varied from 0 to 100 in one-cycle steps and the maximum value of $W(0,\tau)$, with $\tau = N\tau_{\text{cycle}}$, has been recorded. This way, we are not sensitive to the Rabi-like time dependence of the single-particle distribution function, but rather focus on its maximally achievable values, depending on the secondary mode frequency ω_2. The outcome of this setting possesses a very clear resonant behavior [see Fig. 1]. At some specific positions there are peaks achieving maximal values [$W(0,\tau) = 2.0$] after the interaction time τ, whereas less pronounced resonances also occur.

We wish to identify and characterize the resonances in terms of the number of photons, which are absorbed from the strong and perturbative modes. To this end we compute the effective mass $m_* = \lim_{\boldsymbol{p}\to 0}\bar{\varepsilon}_{\boldsymbol{p}}$ defined from the quasi-energy

$$\bar{\varepsilon}_{\boldsymbol{p}} = \frac{1}{2\pi N_{\max}}\int_0^{2\pi N_{\max}} \sqrt{m^2 + [\boldsymbol{p} - e\boldsymbol{\mathcal{A}}(\eta_1)]^2}\, d\eta_1. \tag{23}$$

Here, $N_{\max}$ denotes the plateau length of the bOEF for which the maximal value of $W(0,\tau) \approx 2.0$ is achieved

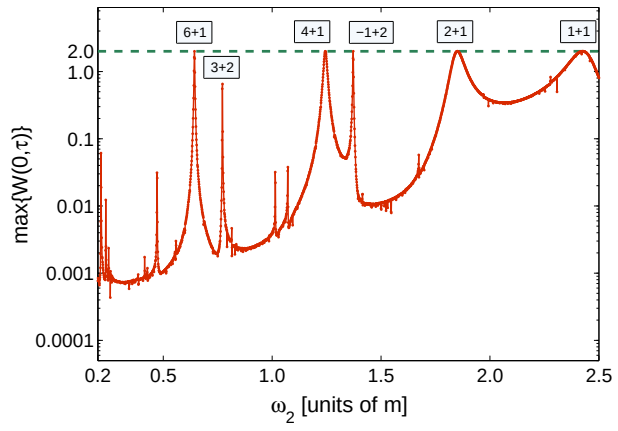

FIG. 1: Resonance spectrum for pair production in a bOEF. Shown are the maximum values of $W(0,\tau)$ (red line) for varying plateau lengths from $N_{\rm plateau} = 0$ to 100 versus the perturbative mode frequency of the field. The maximum possible value of the single-particle distribution function is indicated by the dashed horizontal green line. The remaining field parameters are $\xi_1 = 1.0$, $\xi_2 = 0.1$ and $\omega_1 = 0.3m$. Note the logarithmic scale of the ordinate.

for the first time. It turns out that resonances occur whenever the relation

$$2m_* \approx n_1\omega_1 + n_2\omega_2 \tag{24}$$

is fulfilled, which corresponds to the energy conservation law in Eq. (16) for $\boldsymbol{p} = 0$. This is illustrated in Table I.

We find that the strong field mode dominates the pair-production process in the sense that, in most cases, it contributes more photons than the weak mode. This is because it is easier to absorb photons from the strong than from the weak mode since $\xi_1 \gg \xi_2$. The perturbative mode typically provides just a single photon during the resonant process. Moreover one can observe that n_1 rises in double steps from [2+1] to [4+1] and [6+1] while ω_2 decreases by roughly $\Delta\omega_2 \approx 0.6m$. This coincides with the fact, that these two additional photons, with $\omega_1 = 0.3m$ each, compensate the required energy difference, which confirms the classification scheme based on Eq. (24). Besides, Table I shows that $N_{\rm max}$ is getting substantially larger for decreasing ω_2 along the series of resonances [2+1], [4+1], and [6+1].

It is interesting to note that resonances with $n_2 = 2$ also occur. Since the weak mode enters in second order into these processes, the corresponding peaks are very narrow and the Rabi period becomes long. The latter is evident by the large value of $N_{\rm max}$ for the [3+2] resonance, which we could determine only by substantially increasing the interacting time, and by a comparison of $N_{\rm max}$ for the 3−photon resonances, i. e. [2+1] vs [-1+2]. When the energy ω_2 of the photons from the weak mode is large enough, it even becomes possible that pairs are produced by the absorption of two of them with simultaneous emission of a low-frequency photon from the strong mode. This is exemplified by the resonance [-1+2]. Further peaks, which are not labeled in Fig. 1, do not have the strength to reach the maximum value of $W(0,\tau) \approx 2$ during the range of interaction times under consideration which is restricted by $N_{\rm max} \leq 100$.

TABLE I: Number of photons $n = n_1 + n_2$ versus the perturbative mode frequency ω_2. $N_{\rm max}$ is the plateau length of the bOEF for which the maximal value of $W(0,\tau)$ is achieved for the first time.

$n = n_1+n_2$	ω_2 $[m]$	$N_{\rm max}$	$2m_*$ $[m]$
6+1	0.64293	76	2.4311
4+1	1.24385	16	2.4181
2+1	1.84968	4	2.3775
3+2	0.77160	212	2.4337
-1+2	1.37200	43	2.4285

According to Fig. 1 and Table I, solely odd total photon numbers $n = n_1+n_2$ occur in general. An explanation for this feature can be obtained from the symmetry of charge conjugation (C parity) for real photons. Based on the setting $\boldsymbol{p} = 0$ one can show that the Cparity of the produced pair should be odd [39, 55]. This property can only be realized, if the total number of absorbed photons resembles the same feature, since the charge conjugation of a single photon is also odd. Thus, this real-photon property coincides very well with our photon picture. One has to note, however, that this reasoning does not cover all cases, as the appearance of a [1+1] resonance indicates (see also Fig. 2 in Ref. [39]). Due to its large width, this resonance is not very well defined, though. Therefore we refrain from further discussion of this particular case.

B. Rabi-like oscillations

As shown in Sec. II B, certain frequency combinations exhibit Rabi oscillations with maximal amplitude in the form of $2\sin^2(\Omega_{\rm Rabi}\tau)$ [see Eq. (19)]. This behavior is shown in Fig. 2 for the resonance [4+1] from Table I. To highlight the difference from off-resonant PP processes, we present two more graphs for the nearby frequencies $\omega_2 = 1.22m$ and $\omega_2 = 1.26m$, which lie slightly below and above the resonance, respectively.

From the top curve in Fig. 2 we can extract the corresponding Rabi-like frequency by fitting the $\sin^2$ function from above to the underlying numerical data. In this context, $\Omega_{\rm Rabi}$ is the fit parameter to be determined. Such a procedure, carried out for other resonances as well, leads to the set of values shown in Table II. Since the Rabi-like frequency is inversely proportional to $N_{\rm max}$, we find that $\Omega_{\rm Rabi}$ decreases along the series of resonances [2+1], [4+1], and [6+1]. Besides, the results of our fitting procedure confirm the relation $\Omega_{\rm Rabi} \ll \omega_{1,2}$, which is required for the validity of the resonance condition [39].

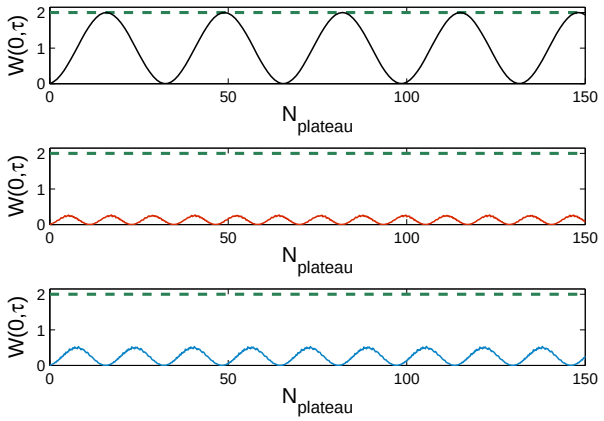

FIG. 2: Resonant Rabi-like oscillation in comparison with off-resonant PP process: The first curve (top to bottom) shows the single-particle distribution function $W(0,\tau)$ versus the plateau length $N_{\rm plateau}$ for the [4+1]-process. The same parameters as in Fig. 1 with $\omega_2 = 1.24385m$ are used. The second and third graphs refer to $\omega_2 = 1.22m$ and $\omega_2 = 1.26m$, respectively, as the perturbative mode frequency of the bOEF .

Resonances also exist for nonzero particle momenta. They can be characterized by the same method, with only the effective mass m_* in Eq. (24) being replaced by the quasienergy $\bar{\varepsilon}_{\boldsymbol{p}}$ of Eq. (23). Our corresponding results will be discussed in the following subsection.

C. Momentum distributions in longitudinal and transversal direction

Further insights into the PP process in a bOEF can be gained from a consideration of the momentum distributions of the created particles. First we shall examine one-dimensional momentum spectra and distinguish between the longitudinal momentum component p_y (along the field) and the transversal momentum component p_x. Recall that an electron of momentum $\boldsymbol{p}$ is always created jointly with a positron of momentum $-\boldsymbol{p}$ and that we have set $p_z = 0$ without loss of generality. We perform our analysis for the field parameters which lead to the [4+1] resonance when the particles have zero momentum. In particular, this means $\omega_2 = 1.24385m$ and $N_{\rm plateau} = 16$. Equations (5) and (6) have been solved for momentum values of p_x and p_y, respectively, varying from 0 to $2.5m$ in steps of $\Delta p = 0.01m$.

Our results are shown by the black solid lines in Figs. 3(a) and 3(b). We notice that for the chosen set of field parameters both curves start at the maximum $W(\boldsymbol{p} = 0,\tau) = 2$. For increasing momenta, the single-particle distribution function generally attains smaller values, whereby for some specific momenta the curves exhibit resonance peaks. By inspection of the corresponding quasienergies one can associate specific numbers of photons with these resonant structures. For the most pronounced peaks, they are compiled in Table III. We note that even total photon numbers now also occur in several cases. The reason is that the previous C-parity selection rule is abrogated by the fact that nonvanishing momenta may lead to nonvanishing orbital angular momenta $\ell \neq 0$. Hence, the C parity of a produced pair may be even.

TABLE II: Rabi-like frequencies for various PP resonances, expressed in units of the fixed frequency $\omega_1 = 0.3m$ of the strong mode and the varying frequency ω_2 of the weak mode, respectively.

$n = n_1+n_2$	ω_2 $[m]$	$\Omega_{\rm Rabi}/\omega_1$	$\Omega_{\rm Rabi}/\omega_2$
6+1	0.64293	0.0033	0.0015
4+1	1.24385	0.0153	0.0037
2+1	1.84968	0.0579	0.0094
3+2	0.77160	0.0012	0.0005
-1+2	1.37200	0.0056	0.0012

Interestingly, for the appearance of a peak, both modes are not always responsible together. This is exemplified by the resonance P10 in Fig. 3(a), whose energy $2\bar{\varepsilon}_{\boldsymbol{p}}$ indicates that it originates from the absorption of nine photons from the strong mode and no photon from the weak mode. This characterization is confirmed by the appearance of the same resonance peak when the weak mode is switched off (red dashed line). Furthermore, we note that some of the observed resonance energies cannot be related uniquely to a specific combination of frequencies. Since the energy of four photons from the strong mode lies close to the energy of a single photon from the weak mode, several peaks are likely to consist of two closely spaced resonances, which are not resolved by our calculations. In particular, the resonances P40 and P50 possess shoulders at the left side of the main peak which may be attributed to the contribution from a second frequency combination. While this phenomenon also occurs in the longitudinal momentum distribution in Fig. 3(b), here the corresponding pairs of resonances at high momenta are resolvable into separate peaks (see P04-P07). We point out that the red dashed line in Fig. 3(b) nicely shows the monofrequent resonances with $n = 9, 10, 11,$ and 12 in the strong OEF mode alone. The blue (grey) solid line also shows a very pronounced resonance (close to the P02 peak) for the case when only the weak mode drives the vacuum decay. It corresponds to the absorption of two high-frequency photons; note that, in contrast to the nearby P02 peak, here the resonance energy at $p_y \approx 0.7m$ amounts to $2\bar{\varepsilon}_{\boldsymbol{p}} \approx 2.44m$ only because the strong mode does not contribute to the field dressing of the energy in Eq. (23).

Comparing Fig. 3(a) with Fig. 3(b), one observes that

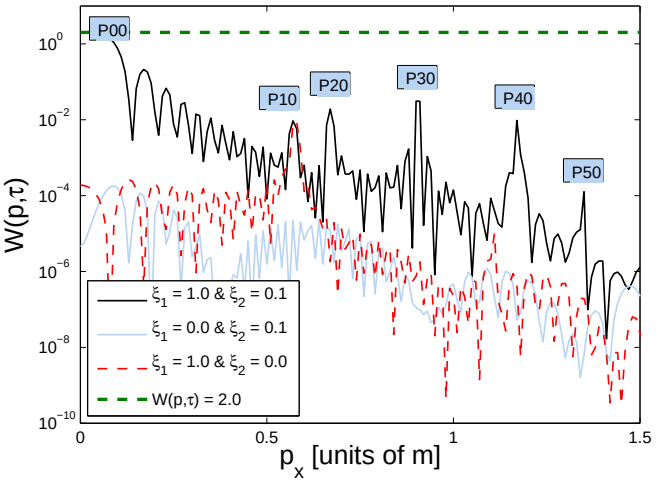

(a) Momentum distribution in transversal direction

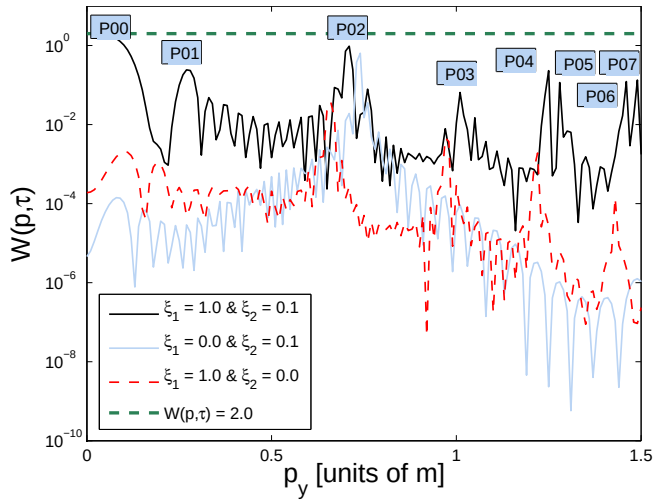

(b) Momentum distribution in longitudinal direction

FIG. 3: One-dimensional momentum distributions of particles created in a bOEF with $\xi_1 = 1.0$, $\xi_2 = 0.1$, $\omega_1 = 0.3m$, $\omega_2 = 1.24385m$, and plateau length $N_{\rm plateau} = 16$ (black solid lines). The single-particle distribution function is plotted on a logarithmic scale versus (a) the transversal momentum p_x and (b) the longitudinal momentum p_y. Resonance peaks are labeled with the relevant photon numbers. For comparison, corresponding momentum distributions of particles produced in mOEFs are also shown where we have set $\xi_1 = 0$ [blue (grey) solid lines] and $\xi_2 = 0$ (red dashed lines), respectively.

large momenta along the transverse direction are, as a general trend, more strongly suppressed than large longitudinal momenta. This can be understood by noting that the latter enter into the quasienergy through the term $p_y - e\mathcal{A}$, so that large values of p_y are partially compensated by the field. Hence, due to the symmetry of the field, it turns out that creating pairs with rather large longitudinal momentum is more likely to occur.

TABLE III: Characterization of resonances in a bOEF as shown in Figs. 3(a) and 3(b) by the numbers of participating photons from the strong and weak modes. The corresponding plateau lengths to reach the maximum, quasienergies and momentum components are also indicated.

Resonance	$n_1 + n_2$	$N_{\rm max}$	$2\bar{\varepsilon}_{\boldsymbol{p}}$ $[m]$	p_x $[m]$	p_y $[m]$
P00	4+1	16	2.4181	0.0	0.0
P10	9+0	213	2.6919	0.5716	0.0
P20	5+1, 1+2	104	2.7810	0.6702	0.0
P30	6+1, 2+2	158	3.0378	0.9049	0.0
P40	7+1, 3+2	332	3.3840	1.1707	0.0
P50	8+1, 4+2	145	3.6392	1.3485	0.0
P01	4+1, 0+2	56	2.4759	0.0	0.2740
P02	5+1, 1+2	30	2.7297	0.0	0.7069
P03	6+1, 2+2	52	3.0392	0.0	1.0114
P04	7+1	73	3.3397	0.0	1.2483
P05	3+2	97	3.3848	0.0	1.2809
P06	8+1	104	3.6410	0.0	1.4581
P07	4+2	96	3.6858	0.0	1.4878

An additional important issue is related to the fact that photon numbers $n_2 > 1$ from the perturbative field mode can occur for some specific momenta (see also Sec. III.A). Moreover it is worth mentioning that almost every determined resonance for nonzero momentum lies quite far below the maximum value of $W(\boldsymbol{p} = 0, \tau) \approx 2$. This is mainly caused by an interaction time which is not sufficiently long to reach the highest possible $W(\boldsymbol{p}, \tau)$ for nonzero momenta; they would be reached for $N_{\rm max} > N_{\rm plateau} = 16$ only (see the third column in Table III). Besides, the finite step size Δp used in our computations may cause a situation in which the position of a resonance is not hit exactly.

Finally, we want to emphasize that in both panels in Fig. 3 the area below $W(\boldsymbol{p}, \tau)$ resulting from a bOEF exceeds those corresponding to the cases driven by a monofrequent OEF (mOEF), which are shown for comparison. These patterns already provide evidence that the density of created pairs can be substantially enhanced by superimposing a perturbative high-frequency mode onto a strong low-frequency mode.

D. Two-dimensional momentum distribution

While in the previous subsection the momentum dependence of the single-particle distribution function was studied for the longitudinal and transversal directions, now we shall examine in a more general way the two-dimensional momentum distribution in the (p_x, p_y) plane. This way, all intermediate directions are covered. We vary both p_x and p_y in the interval from $-2.5m$ to $2.5m$. The field parameters are chosen again as $\xi_1 = 1.0$, $\xi_2 = 0.1$, $\omega_1 = 0.3m$, $\omega_2 = 1.24385m$, and $N_{\rm plateau} = 16$.

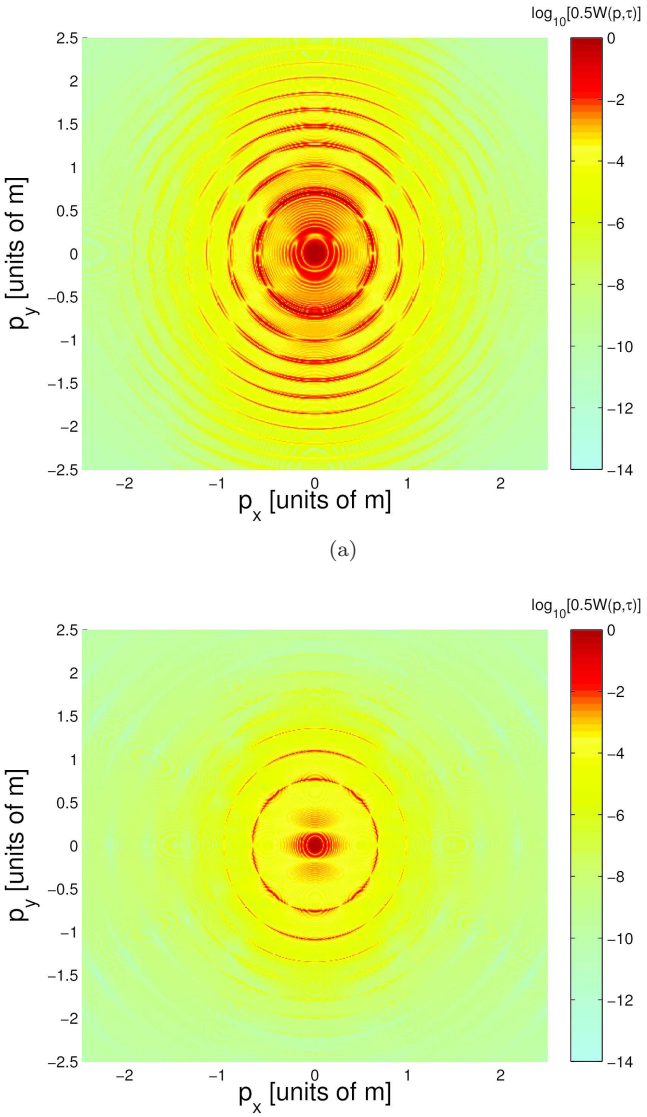

FIG. 4: Two-dimensional momentum distributions in the (p_x, p_y) plane for pair production in (a) a bOEF [$\xi_1 = 1.0$, $\xi_2 = 0.1$, $\omega_1 = 0.3m$, $\omega_2 = 1.24385m$, and $N_{\rm plateau} = 16$] and (b) mOEF [$\xi_1 = 1.0$, $\omega_1 = 0.34888m$, and $N_{\rm plateau} = 45$]. In the center of both panels a maximum is achieved. While in (a) this maximum is characterized by the [4+1]-process, in (b) it is despicted by the [7]-process. Observe that the single-particle distribution function is plotted in the form $\log_{10}[\frac{1}{2}W(\boldsymbol{p},\tau)]$.

They lead to a [4+1] resonance with maximal probability at the point $p_x = p_y = 0$. The corresponding distribution is shown in Fig. 4(a) in a color-coded scheme. The logarithmic quantity $\log_{10}[\frac{1}{2}W(\boldsymbol{p},\tau)]$ has been plotted. We observe ring-shaped regions of high probability which reflect the resonance properties of the process. Cuts along the p_x (p_y) axis at $p_y = 0$ ($p_x = 0$) would reproduce the one-dimensional momentum distributions along the transversal (longitudinal) directions shown in Fig. 3. This way, the resonance rings can be characterized in terms of the numbers n_1 and n_2 of participating photons. We note that the ring-shaped structures are slightly elongated in the longitudinal direction. This is because large values of p_y are more likely to occur than large values of p_x, as was mentioned before.

It is interesting to compare the two-dimensional momentum distribution in a bOEF with that in a mOEF. To this end, we use the following mOEF parameters $\xi_1 = 1.0$, $\omega_1 = 0.34888m$ and $N_{\rm plateau} = 45$, which also lead to a resonance with maximum probability at $p_x = p_y = 0$. It corresponds to the absorption of $n = 7$ photons (see Table I in Ref. [39]). Figure 4(b) presents the corresponding two-dimensional distribution function on the same color-coded logarithmic scale. We observe similar ring-shaped structures, with the expected [7] resonance in the center. This one is surrounded by further less pronounced resonances for increasing photon numbers $n = 8, 9, 10, \ldots$, a fact which resembles some finding of Ref. [56]. They fulfill the monofrequent resonance condition $2\bar{\varepsilon}_{\boldsymbol{p}} \approx n\omega_1$. A rather remarkable trait is the distance between the resonance rings. By comparing Figs. 4(a) and 4(b) it becomes evident that for the bOEF, these are more closely spaced than for the mOEF. The reason is that the presence of a second frequency in the case of a bOEF offers more options to fulfill the resonance condition in Eq. (24) than in the monofrequent case. One can observe, moreover, that the number of resonance rings with sizeable magnitudes is increased in the presence of a bOEF. This indicates that the total pair yield, which is obtained by integration over the momentum space, will be substantially larger in the bOEF. This becomes especially apparent in view of the considerably larger red-colored regions in Fig. 4(a).

E. Total number of electron-positron pairs

From the two-dimensional momentum distributions in the (p_x, p_y) plane, we can obtain the total number of produced electron-positron pairs per unit volume by evaluating the integral (10). We can exploit the cylindrical symmetry of the problem about the y axis and, accordingly, perform the integral over d^3p in cylindrical coordinates using $|p_x|$ as the polar coordinate. For a finite interaction time τ, we thus arrive at the expression

$$\mathcal{N}_{e^-e^+} = \frac{1}{4\pi^2}\int_{-\infty}^{\infty}\int_{0}^{\infty} W(p_x, p_y, 0, \tau)|p_x|dp_x dp_y. \quad (25)$$

For the numerical evaluation, it is required to introduce a finite cutoff for such values in the momentum plane where the distribution function no longer contributes appreciably. We shall use the cutoff value $\bar{p} = 3m$ and restrict the ranges of integration to $|p_x| \leq \bar{p}$ and $|p_y| \leq \bar{p}$. Hence,

we obtain approximately

$$\mathcal{N}_{e^-e^+} \approx \frac{1}{8\pi^2}\int_{-\bar{p}}^{+\bar{p}}\int_{-\bar{p}}^{+\bar{p}} W(p_x,p_y,0,\tau)|p_x|dp_x dp_y, \quad (26)$$

where we have exploited the symmetry relation $W(-p_x,p_y,0,\tau) = W(+p_x,p_y,0,\tau)$ in order to make the connection of the total number of produced pairs with the two-dimensional momentum distributions, as illustrated in Fig. 4, explicit. The latter integral is solved by numerical integration as a sum of the corresponding discretized values provided by the two-dimensional data sets.

First, we analyze the dependence of the total number of produced pairs on the strong-field intensity parameter of a bOEF. The latter has been varied within the interval $0.3 \leq \xi_1 \leq 1.4$. The other parameters were set to $\omega_1 = 0.3m$, $\omega_2 = 1.24385m$, $\xi_2 = 0.1$ and $N_{\text{plateau}} = 45$. The number of plateau cycles has been chosen to enable a good comparison with the mOEF case.[7] The latter was realized by using parameters identical to the strong mode of the bOEF. The respective plot for the total number of produced electron-positron pairs per unit volume (given by the Compton volume $V_C = m^{-3}$) is shown in Fig. 5(a).

We observe that throughout the whole range of ξ_1 values, the pair yield from the bOEF is substantially larger than that from the mOEF. This indicates an effective enhancement of the pair production by superimposing a second weak mode of high frequency in addition to a stronger one. In particular, when $\xi_1 \ll 1$, the bOEF results exceed the mOEF results by 5 orders of magnitude. The (average) slope of the mOEF curve, however, is larger than the bOEF curve (see also Refs. [19, 23, 28, 29]), so that eventually for $\xi_1 \gg 1$ the enhancing effect of the perturbative mode will diminish. This behavior coincides with the intuitive expectation according to which the perturbative high-frequency mode is getting less relevant because the low-frequency mode becomes strong enough to dominate the production process.

Another noticeable issue shown in Fig. 5(a) is the comparison for the mOEF case between the numerical results and the analytical curve obtained from Ref. [14]. The general trend of both curves is very similar, with the caveat that their absolute heights are somewhat different (see also Fig. 14 in Ref. [39]). A remarkable feature of the numerical curve is that it exhibits considerable dropoffs around the values of $\xi_1 \approx 0.5$, 0.95, and 1.32, which do not occur for the analytical curve. They can be attributed to the fact that at these specific ξ_1 values a resonance disappears due to energetic reasons. Namely, when ξ_1 increases, the effective mass m_* increases as well, which determines the minimal energy to be absorbed from the field in order to produce a pair. This phenomenon is commonly known as a channel-closing effect (see, e.g., Ref. [57, 58]). The positions of the channel closings are marked by the vertical dashed lines in Fig. 5(a). From left to right, they correspond to the vanishing of the resonances with $n = 7$, 8, and 9, respectively.

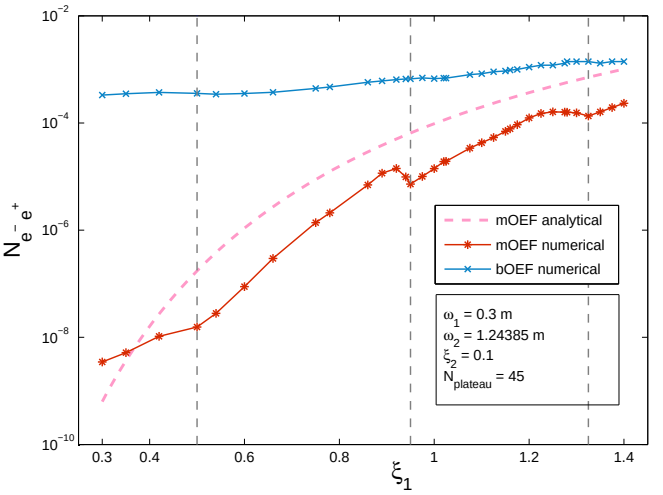

(a) Dependence on the strong-field intensity parameter for bOEF versus mOEF.

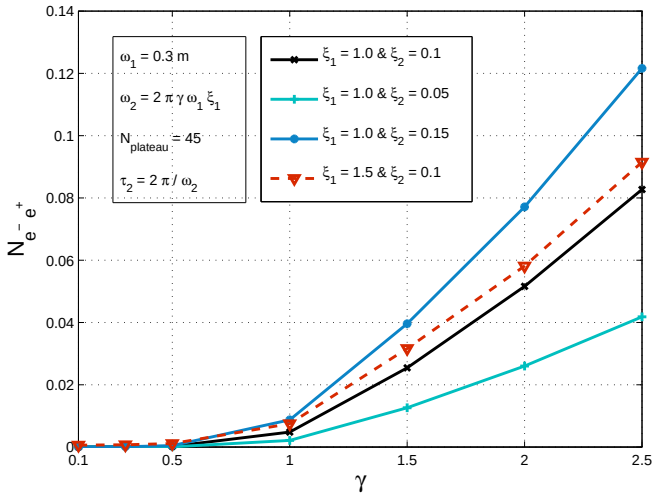

(b) Dependence on the combined Keldysh parameter for various bOEFs.

FIG. 5: Total number of electron-positron pairs produced in a unit volume V_C. Panel (a) shows the dependence on the strong-field intensity parameter ξ_1 for a bOEF with parameters as indicated in the legend (blue crosses). For comparison, corresponding numerical results for a mOEF (obtained by setting $\xi_2 = 0$) are shown (red asterisks), as well as the analytical prediction from Ref. [14] (pink dashed line). The vertical grey dashed lines mark positions where channel closings for the mOEF appear. Panel (b) shows the dependence on the combined Keldysh parameter $\gamma = m/(eE_1\tau_2)$.

Finally, in addition to the previous discussion,

[7] Note that, since $N_{\max} = 16$ for the bOEF according to Table I, the pair production probability will reach its next maximum close to $N_{\text{plateau}} = 45$, due to the periodic Rabi oscillations.

Fig. 5(b) shows the dependency of the total number of produced pairs per unit volume V_C on the combined Keldysh parameter given by $\gamma = \frac{m}{eE_1\tau_2}$, where $\tau_2 = 2\pi/\omega_2$ is the period of the perturbative mode. The interval $0.1 \leq \gamma \leq 2.5$ is considered and the Keldysh parameter is varied by varying ω_2 while keeping E_1 fixed. The curve for $\xi_1 = 1.0$, $\xi_2 = 0.1$ (black solid line) may serve us as a reference. By comparison we find that, when the intensity parameter of the weak mode is amplified by a factor of 1.5 (blue solid line), a much stronger growth of the particle number results as compared with the case when the intensity parameter of the strong mode is increased by the same factor (red dashed line). Thus, in the considered interaction regime, it is more efficient to invest in an increase of the small parameter ξ_2 than a further increase of the large parameter ξ_1.

Moreover, a comparison of the solid lines in Fig. 5(b) reveals that the particle number scales linearly with ξ_2. From our formalism, this can be understood by inspection of Eq. (9). The total electric field $E(t) = E_1(t) + E_2(t)$ enters quadratically there, and since we operate in a regime where the combined effect of both modes is crucial, one may expect that the resulting cross term $\sim E_1(t)E_2(t)$ gives the largest contribution to the single-particle distribution function. This leads to a linear dependence on E_2, in accordance with the numerical outcomes.

We would like to stress that, despite its very plausible explanation, the linear scaling with the parameter ξ_2 is an interesting feature of PP in a bOEF. In fact, other PP processes, which exhibit a similar enhancement mechanism in a bifrequent field, do not share this scaling property. For dynamically assisted Breit-Wheeler [28] as well as Bethe-Heitler [23, 29] PP in strong laser fields, a quadratic scaling law $\sim \xi_2^2$ has been found, provided that a single high-frequency photon assists in the process. This is because the underlying PP amplitude there is linear in ξ_2 whose square provides the PP rate. That a subquadratic dependence on ξ_2 arises in a bOEF can already be anticipated on the basis of its resonant nature, which does not exist for the PP processes in Refs. [23, 28, 29]. The resonances provide a substantial contribution to the total number of produced pairs, but their height is bounded by the maximum value of $W(\boldsymbol{p}, \tau) = 2$. Thus, an increase of ξ_2 cannot enhance this value further. However, the fundamental reason for the different ξ_2 scaling in a bOEF as compared with intense bifrequent laser fields [23, 28, 29] can be traced back to the fact that the strong mode of the bOEF alone is capable of producing pairs, whereas the quantum vacuum is stable in the presence of a plane-wave laser field. Therefore, in the latter case, the leading-order vacuum polarization diagram, whose imaginary part is related to the PP rate via the optical theorem, contains the perturbatively weak field at two vertices. In contrast, to the PP in an OEF also diagrams with just a single perturbative vertex contribute, which leads to the observed linear dependence on the small parameter ξ_2.

IV. CONCLUSION

We presented a comprehensive investigation of electron-positron pair production in a bifrequent OEF composed of a strong low-frequency and a perturbative high-frequency mode. A quantum kinetic approach allowed us to calculate the single-particle distribution function by using numerical methods. We found a pronounced resonant behavior depending on the frequency composition of the field and demonstrated Rabi-like oscillations in full time resolution on and slightly off a resonance peak (Secs. III A and III B). These numerical findings showed a clear agreement with predictions from the theory [Sec. II B]. The occurrence of the resonances could be explained by discrete numbers of photons absorbed from (or emitted into) the bifrequent field. While in the case of vanishing particle momenta, only odd total photon numbers are allowed due to charge-conjugation symmetry, resonant production of pairs with nonzero momenta may also proceed involving an even number (Secs. III C and III D). Besides, it has been shown that processes with more than one photon from the perturbative mode also occur. Finally, we have seen that the superimposed perturbative mode can substantially amplify the total number of generated electron-positron pairs in comparison with the case where a single strong mode drives the vacuum decay (Sec. III E). The enhancement shows a linear dependence on the intensity parameter of the weak mode and is especially pronounced at large values of the relative Keldysh parameter (i.e., at relatively low field strengths of the strong mode and high frequencies of the weak mode).

Acknowledgments

S. Villalba-Chávez gratefully acknowledges the support of the Alexander von Humboldt Foundation in the early stage of this project.

Appendix A: Remarks on the second quantization

This appendix provides some details about the second quantization formalism in a time-dependent electric field of the form $\boldsymbol{E}(t) = (0, E(t), 0)$. To begin with, we remark that the action of the creation operators $a^\dagger_{\boldsymbol{p},s}(t)$ and $b^\dagger_{-\boldsymbol{p},s}(t)$ on the instantaneous vacuum state $|\mathrm{VAC}, t\rangle$ of the theory, defined by

$$a_{\boldsymbol{p},s}(t)|\mathrm{VAC}, t\rangle = b_{-\boldsymbol{p},s}(t)|\mathrm{VAC}, t\rangle = 0 \,, \tag{A1}$$

allows us to build up a Fock space for the quasiparticles. A connection between the previous set of states and those resulting at $t \to t_{\mathrm{in}}$ can be established by means of a canonical unitary operator $\mathcal{U}(t, t_{\mathrm{in}})$ so that

$$|\mathrm{VAC}, t\rangle = \mathcal{U}(t, t_{\mathrm{in}})|\mathrm{VAC}, \mathrm{in}\rangle, \tag{A2}$$

where the ground state $|\mathrm{VAC},\mathrm{in}\rangle$ is defined in the Heisenberg picture by $a_{\mathrm{in}}|\mathrm{VAC},\mathrm{in}\rangle = b_{\mathrm{in}}|\mathrm{VAC},\mathrm{in}\rangle = 0$ with $a_{\mathrm{in}} \equiv a_{\boldsymbol{p},s}$ and $b_{\mathrm{in}} \equiv b_{-\boldsymbol{p},s}$ at $t \to t_{\mathrm{in}}$. With these details in mind and by considering Eq. (A2), the following transformation properties are obtained:

$$a_{\boldsymbol{p},s}(t) = \mathcal{U}(t,t_{\mathrm{in}})a_{\mathrm{in}}\,\mathcal{U}^{\dagger}(t,t_{\mathrm{in}}), \tag{A3}$$

$$b^{\dagger}_{-\boldsymbol{p},s}(t) = \mathcal{U}^{\dagger}(t,t_{\mathrm{in}})b^{\dagger}_{\mathrm{in}}\,\mathcal{U}(t,t_{\mathrm{in}}). \tag{A4}$$

The structure of the evolution operator $\mathcal{U}(t,t_{\mathrm{in}})$ has been investigated in Refs. [7, 59, 60]. Its construction can be carried out by following a procedure similar to that established in the context of the BCS theory (for further details, we refer the reader to Ref. [61] and references therein). Following the ansatz of these references, we express $\mathcal{U}(t,t_{\mathrm{in}})$ in the following form:

$$\begin{aligned}&\mathcal{U}(t,t_{\mathrm{in}}) = \exp[\Lambda(t,t_{\mathrm{in}})], \quad \Lambda(t,t_{\mathrm{in}}) = \sum_{\boldsymbol{p},s}\Lambda_{\boldsymbol{p},s}(t,t_{\mathrm{in}}),\\ &\Lambda_{\boldsymbol{p},s}(t,t_{\mathrm{in}}) = \alpha a^{\dagger}_{\mathrm{in}}b^{\dagger}_{\mathrm{in}} - \alpha^{*}b_{\mathrm{in}}a_{\mathrm{in}} + i\beta a^{\dagger}_{\mathrm{in}}a_{\mathrm{in}} - i\beta b_{\mathrm{in}}b^{\dagger}_{\mathrm{in}}\end{aligned} \tag{A5}$$

where the respective complex and real parameters α and β are functions of $\boldsymbol{p}$ and t. It is worth mentioning at this point that the above operator $\mathcal{U}(t,t_{\mathrm{in}})$ preserves both the unitary and the canonic features. To establish the relation between α and the coefficient arising from the Bogolyubov transformations, we Taylor-expand all instances of $\mathcal{U}(t,t_{\mathrm{in}})$ in Eq. (A3) so that

$$\begin{aligned}a_{\boldsymbol{p},s}(t) &= \sum_{n=0}^{\infty}\frac{1}{n!}\left[\Lambda,[\Lambda,\ldots[\Lambda,a_{\mathrm{in}}]\ldots]\right],\\ b^{\dagger}_{-\boldsymbol{p},s}(t) &= \sum_{n=0}^{\infty}\frac{1}{n!}\left[\Lambda,\left[\Lambda,\ldots\left[\Lambda,b^{\dagger}_{\mathrm{in}}\right]\ldots\right]\right].\end{aligned} \tag{A6}$$

As a consequence of a reiterated use of the commutation rules $[\Lambda,a_{\mathrm{in}}] = -\alpha b^{\dagger}_{\mathrm{in}} - i\beta a_{\mathrm{in}}$, $[\Lambda,b_{\mathrm{in}}] = \alpha a^{\dagger}_{\mathrm{in}} - i\beta b_{\mathrm{in}}$, $[\Lambda,a^{\dagger}_{\mathrm{in}}] = -\alpha^{*}b_{\mathrm{in}} + i\beta a^{\dagger}_{\mathrm{in}}$ and $[\Lambda,b^{\dagger}_{\mathrm{in}}] = \alpha^{*}a_{\mathrm{in}} + i\beta b^{\dagger}_{\mathrm{in}}$, we can reduce the above relations to

$$\begin{bmatrix} a_{\boldsymbol{p},s}(t) \\ b^{\dagger}_{-\boldsymbol{p},s}(t)\end{bmatrix} = \begin{bmatrix} g^{*}(\boldsymbol{p},t) & f(\boldsymbol{p},t) \\ -f^{*}(\boldsymbol{p},t) & g(\boldsymbol{p},t)\end{bmatrix}\begin{bmatrix} a_{\mathrm{in}} \\ b^{\dagger}_{\mathrm{in}}\end{bmatrix}, \tag{A7}$$

where the unknown matrix elements

$$f(\boldsymbol{p},t) = -\frac{\alpha}{\sqrt{|\alpha|^2+\beta^2}}\sin(\sqrt{|\alpha|^2+\beta^2}), \tag{A8}$$

$$g(\boldsymbol{p},t) = \cos(\sqrt{|\alpha|^2+\beta^2}) + i\frac{\beta}{\alpha}f(\boldsymbol{p},t) \tag{A9}$$

clearly satisfy the condition $|g(\boldsymbol{p},t)|^2 + |f(\boldsymbol{p},t)|^2 = 1$.

Let us turn our attention to the connection between the in− and the instantaneous ground states [Eq. (A2)]. When $\mathcal{U}(t,t_{\mathrm{in}})$ is Taylor-expanded, its action on $|\mathrm{VAC},\mathrm{in}\rangle$ involves a rather complicated mixture of the second quantization operators a_{in}, b_{in}, $a^{\dagger}_{\mathrm{in}}$, $b^{\dagger}_{\mathrm{in}}$. To avoid this problem, we disentangle the evolution operator according to the rule $\mathcal{U}(t,t_{\mathrm{in}}) = \prod_{\boldsymbol{p},s}\exp[\Lambda_{\boldsymbol{p},s}(t,t_{\mathrm{in}})]$. This step is allowed due to the fact that the commutator between two arbitrary elements $\Lambda_{\boldsymbol{p},s}(t,t_{\mathrm{in}})$ and $\Lambda_{\boldsymbol{p}',s'}(t,t_{\mathrm{in}})$ vanishes identically. Next, we expand $\exp[\Lambda_{\boldsymbol{p},s}(t,t_{\mathrm{in}})]$ and use the identities $\Lambda^{2n+1}_{\boldsymbol{p},\sigma}(t,t_{\mathrm{in}}) = (-1)^n(|\alpha|^2+\beta^2)^n\Lambda_{\boldsymbol{p},\sigma}(t,t_{\mathrm{in}})$ and $\Lambda^{2n}_{\boldsymbol{p},\sigma}(t,t_{\mathrm{in}}) = (-1)^{n-1}(|\alpha|^2+\beta^2)^{n-1}\Lambda^{2}_{\boldsymbol{p},\sigma}(t,t_{\mathrm{in}})$ with $\Lambda^{2}_{\boldsymbol{p},\sigma}(t,t_{\mathrm{in}}) = -(|\alpha|^2+\beta^2)(b^{\dagger}_{\mathrm{in}}b_{\mathrm{in}}a^{\dagger}_{\mathrm{in}}a_{\mathrm{in}} + b_{\mathrm{in}}b^{\dagger}_{\mathrm{in}}a_{\mathrm{in}}a^{\dagger}_{\mathrm{in}})$ to express the instantaneous ground state of the theory as a two-mode squeezed state of the in−particle pairs

$$|\mathrm{VAC},t\rangle = \prod_{\boldsymbol{p},s}g^{*}(\boldsymbol{p},t)\exp\left[\frac{f(\boldsymbol{p},t)}{g^{*}(\boldsymbol{p},t)}b^{\dagger}_{\mathrm{in}}a^{\dagger}_{\mathrm{in}}\right]|\mathrm{VAC},\mathrm{in}\rangle. \tag{A10}$$

Considering this expression, it is quite simple to verify that the vacuum persistence probability is given by

$$\begin{aligned}\mathcal{P}_{\mathrm{vac}}(t) &= |\langle\mathrm{VAC},t|\mathrm{VAC},\mathrm{in}\rangle|^2 = \exp\sum_{\boldsymbol{p},s}\ln\left[g(\boldsymbol{p},t)^2\right]\\ &= \exp\left[(t-t_{\mathrm{in}})V\Gamma_{\mathrm{vac}}(t)\right],\end{aligned} \tag{A11}$$

where $\Gamma_{\mathrm{vac}}(t)$ denotes the instantaneous rate of vacuum decay per unit of volume:

$$\begin{aligned}\Gamma_{\mathrm{vac}}(t) &= \frac{\ln[\mathcal{P}_{\mathrm{vac}}(t)]}{(t-t_{\mathrm{in}})V}\\ &= \frac{2}{t-t_{\mathrm{in}}}\int \mathrm{d}^3p\ln\left(1-|f(\boldsymbol{p},t)|^2\right).\end{aligned} \tag{A12}$$

This last expression results from the transition to the infinite volume continuum limit in which the relation $\frac{1}{V}\sum_{\boldsymbol{p}} \to \int \mathrm{d}^3p$ with $\mathrm{d}^3 \equiv d^3/(2\pi)^3$ holds. The factor of 2 in Eq. (A12) results from the sum over the discrete spin variable s. In the subcritical regime [$E \ll E_c$], the use of the above expression allows us to reproduce the vacuum decay rate $\Gamma_{\mathrm{vac}} = \frac{(eE)^2}{4\pi^3}\sum_{n=1}^{\infty}\frac{1}{n^2}\exp[-\pi\frac{E_c}{E}]$ found by Schwinger for a constant electric field. A detailed calculation of this subject can be found in [43].

Appendix B: Deriving the Boltzmann-Vlasov equation

The integrodifferential representation of the quantum kinetic equation for the PP process [Eq. (9)] is determined only after performing some additional steps in Eqs. (5) and (6). To this end, we determine the temporal equations of new variables $\bar{f}(\boldsymbol{p},t)$ and $\bar{g}(\boldsymbol{p},t)$, which are linked to the original coefficients $f(\boldsymbol{p},t)$ and $g(\boldsymbol{p},t)$ through unitary transformations $\bar{f}(\boldsymbol{p},t) = -if(\boldsymbol{p},t)\exp\left[i\int_{t_0}^{t}dt'\,a_{\boldsymbol{p}}(t')\right]$ and $\bar{g}(\boldsymbol{p},t) = ig(\boldsymbol{p},t)\exp\left[-i\int_{t_0}^{t}dt'\,a_{\boldsymbol{p}}(t')\right]$. These details, together with Eqs. (5) and (6), allow us to establish the system of ODEs given by Eq. (11) and Eq. (12):

$$\dot{\bar{f}}(\boldsymbol{p},t) = -\frac{1}{2}Q_{\boldsymbol{p}}(t)\bar{g}(\boldsymbol{p},t)\exp\left[2i\Theta_{\boldsymbol{p}}(t)\right], \tag{B1}$$

$$\dot{\bar{g}}(\boldsymbol{p},t) = \frac{1}{2}Q_{\boldsymbol{p}}(t)\bar{f}(\boldsymbol{p},t)\exp\left[-2i\Theta_{\boldsymbol{p}}(t)\right] \tag{B2}$$

with $Q_{\boldsymbol{p}}(t)$ and $\Theta_{\boldsymbol{p}}(t)$ being defined as

$$Q_{\boldsymbol{p}}(t) = \frac{eE(t)\epsilon_\perp}{w_{\boldsymbol{p}}^2(t)}, \quad \Theta_{\boldsymbol{p}}(t) = \int_{t_0}^{t} dt' \; w_{\boldsymbol{p}}(t'). \tag{B3}$$

In this framework, the initial conditions $\bar{f}(\boldsymbol{p}, -\infty) = 0$ and $\bar{g}(\boldsymbol{p}, -\infty) = 1$ ensure the pure vacuum condition. At this point it is convenient to look at the time evolution equations of the single-particle distribution function Eq. (4) and the quasiparticle correlation function $O(\boldsymbol{p}, t) = \sum_s \langle \mathrm{VAC}, \mathrm{in} | b^\dagger_{-\boldsymbol{p},s}(t) a^\dagger_{\boldsymbol{p},s}(t) | \mathrm{VAC}, \mathrm{in} \rangle = 2f(\boldsymbol{p}, t) g^*(\boldsymbol{p}, t)$. With the help of Eqs. (B1) and (B2), we find that

$$\dot{W}(\boldsymbol{p}, t) = -Q_{\boldsymbol{p}}(t) \mathrm{Re} \left\{ O(\boldsymbol{p}, t) \exp\left[-2i\Theta_{\boldsymbol{p}}(t)\right] \right\}, \tag{B4}$$

$$\dot{O}(\boldsymbol{p}, t) = -Q_{\boldsymbol{p}}(t) \left[1 - W(\boldsymbol{p}, t)\right] \exp\left[2i\Theta_{\boldsymbol{p}}(t)\right]. \tag{B5}$$

Next, we integrate the second expression in Eq. (B5) over time from $-\infty$ to t and insert the resulting expression for $O(\boldsymbol{p}, t)$ into Eq. (B4) afterwards. The outcome of this procedure is the Boltzmann-Vlasov equation [Eq. (9)].

[1] F. Sauter, Z. Phys. **69**, 742 (1931).
[2] W. Heisenberg and H. Euler, Z. Phys. **98**, 714 (1936).
[3] J. S. Schwinger, Phys. Rev. **82**, 664 (1951).
[4] See http://www.eli-beams.eu/.
[5] See http://www.xcels.iapras.ru/.
[6] A. Casher *et* al., Phys. Rev. D **20**, 179 (1979).
[7] E. S. Fradkin, D. M. Gitman, and S. M. Shvartsman, *Quantum Electrodynamics with Unstable Vacuum* (Springer-Verlag, Berlin, 1991).
[8] G. V. Dunne, in *From fields to strings*, edited by M. Shifman *et al.*, (World Scientific Publishing, Singapore, 2005), Vol. 1, pp. 445-522; [hep-th/0406216].
[9] M. Ruf, G. R. Mocken, C. Müller, K. Z. Hatsagortsyan, and C. H. Keitel, Phys. Rev. Lett **102**, 080402 (2009).
[10] F. Hebenstreit, R. Alkofer, and H. Gies, Phys. Rev. D **82**, 105026 (2010); [arXiv:1007.1099[hep-ph]].
[11] F. Hebenstreit, R. Alkofer, and H. Gies, Phys. Rev. Lett. **107**, 180403 (2011) [arXiv:1106.6175 [hep-ph]].
[12] F. Hebenstreit, J. Berges, and D. Gelfand, Phys. Rev. D **87**, 105006 (2013) [arXiv:1302.5537 [hep-ph]].
[13] D. Berényi, S. Varró, V. V. Skokov, and P. Lvai, "Pair production at the edge of the QED flux tube," [arXiv:1401.0039 [hep-ph]].
[14] E. Brezin, and C. Itzykson, Phys. Rev. D **2**, 1191 (1970).
[15] Y. I. Salamin, S. Hu, K. Z. Hatsagortsyan, and C. H. Keitel, Phys. Rep. **427**, 41 (2006), Sec. 7.1.3.
[16] S. M. Schmidt, D. Blaschke, G. Röpke, S. A. Smolyansky, and A. V. Prozorkevich, Int. J. Mod. Phys. E **07**, 709 (1998); [hep-ph/9809227].
[17] S. M. Schmidt, D. Blaschke, G. Röpke, A. V. Prozorkevich, S. A. Smolyansky, and V. D. Toneev, Phys. Rev. D **59**, 094005 (1999).
[18] R. Alkofer, M. B. Hecht, C. D. Roberts, S. M. Schmidt, and D. V. Vinnik Phys. Rev. Lett. **87**, 193902 (2001); [nucl-th/0108046].
[19] R. Schützhold, H. Gies, and G. Dunne, Phys. Rev. Lett **101**, 130404 (2008). [arXiv:0807.0754 [hep-th]].
[20] G. Dunne, H. Gies, and R. Schützhold, Phys. Rev. D **80**, 111301 (2009). [arXiv:0908.0948 [hep-ph]].
[21] C. Müller, A. B. Voitkiv, and N. Grün. Phys. Rev. A **67**, 063407 (2003).
[22] P. Sieczka, K. Krajewska, J. Z. Kamiński, P. Panek, and F. Ehlotzky, Phys. Rev. A **73**, 053409 (2006).
[23] A. Di Piazza, E. Lötstedt, A. I. Milstein, and C. H. Keitel, Phys. Rev. Lett. **103**, 170403 (2009); [arXiv:0906.0726 [hep-ph]].
[24] S. S. Bulanov, T. Z. Esirkepov, A. G. R. Thomas, J. K. Koga, and S. V. Bulanov, Phys. Rev. Lett **105**, 220407 (2010); [arXiv:1007.4306 [physics.plasm-ph]].
[25] M. Jiang, W. Su, Z. Q. Lv, X. Lu, Y. J. Li, R. Grobe, and Q. Su, Phys. Rev. A **85**, 033408 (2012).
[26] M. Jiang, Q. Z. Lv, Z. M. Sheng, R. Grobe, and Q. Su, Phys. Rev. A **87**, 042503 (2013).
[27] A. I. Titov, B. Kämpfer, H. Takabe, and A. Hosaka, Phys. Rev. A **87**, 042106 (2013).
[28] M. J. A. Jansen and C. Müller, Phys. Rev. A **88**, 052125 (2013).
[29] S. Augustin and C. Müller, Phys. Lett. B **737**, 114 (2014).
[30] Z. L. Li, D. Lu, B. S. Xie, L. B. Fu, J. Liu, and B. F. She, Phys. Rev. D **89**, 093011 (2014).
[31] D. L. Burke *et al.*, Phys. Rev. Lett. **79**, 1626 (1997).
[32] M. Orthaber, F. Hebenstreit, and R. Alkofer, Phys. Lett. B **698**, 80 (2011); [arXiv:1102.2182 [hep-ph]].
[33] C. Fey and R. Schützhold, Phys. Rev. D **85**, 025004 (2012); [arXiv:1110.5499 [hep-th]].
[34] V. S. Popov, JETP Lett. **18**, 255 (1973).
[35] F. Hebenstreit, R. Alkofer, G. Dunne, and H. Gies, Phys. Rev. Lett. **102**, 150404 (2009); [arXiv:0901.2631 [hep-ph]].
[36] E. Akkermans and G. V. Dunne, Phys. Rev. Lett. **108**, 030401 (2012).
[37] N. B. Narozhnyĭ and A. I. Nikishov, Sov. Phys. JETP **38**, 427 (1974).
[38] H. K. Avetissian, A. K. Avetissian, G. F. Mkrtchian, and Kh. Sedrakian, Phys. Rev. E **66**, 016502 (2002).
[39] G. R. Mocken, M. Ruf, C. Müller, and C. H. Keitel, Phys. Rev. A **81**, 022122 (2010).
[40] K. Krajewska and J. Z. Kamiński, Phys. Rev. A **86**, 021402 (2012).
[41] Y. B. Wu and S. S. Xue, Phys. Rev. D **90**, 013009 (2014).
[42] A. M. Fedotov, N. B. Narozhny, G. Mourou, and G. Korn, Phys. Rev. Lett. **105**, 080402 (2010); [arXiv:1004.5398 [hep-ph]].
[43] N. Tanji, Ann. Phys. (Amsterdam) **324**, 1691 (2009); [arXiv:0810.4429 [hep-ph]].
[44] J. C. R. Bloch, V. A. Mizerny, A. V. Prozorkevich, C. D. Roberts, S. M. Schmidt, S. A. Smolyansky, and D. V. Vinnik, Phys. Rev. D **60**, 116011 (1999); [nucl-th/9907027].
[45] D. V. Vinnik, A. V. Prozorkevich, S. A. Smolyansky, V. D. Toneev, C. D. Roberts, and S. M. Schmidt, Eur. Phys. J. C **22**, 341 (2001); [nucl-th/0103073].
[46] H. Bacry, P. Combe, and J. L. Richard, Nuovo Cimento

A **67**, 267 (1970).
[47] S. Villalba-Chávez and A. E. Shabad, Phys. Rev. D **86**, 105040 (2012); arXiv:1206.4491 [hep-th].
[48] J. L. Richard, Nuovo Cimento A **8**, 485 (1972).
[49] S. Weinberg, *The Quantum Theory of Fields* (Cambridge University Press, Cambridge, England, 2001).
[50] D. V. Vinnik, R. Alkofer, S. M. Schmidt, S. A. Smolyansky, V. V. Skokov, and A. V. Prozorkevich, Few-Body Syst. **32**, 23 (2002).
[51] F. Hebenstreit, R. Alkofer, and H. Gies, Phys. Rev. D **78**, 061701(R) (2008); [arXiv:0807.2785 [hep-ph]].
[52] R. Dabrowski and G. V. Dunne, Phys. Rev. D **90**, 025021 (2014).
[53] D. B. Blaschke, B. Kämpfer, A. D. Panferov, A. V. Prozorkevich, and S. A. Smolyansky, Contrib. Plasma Phys. **53**, 165 (2013).
[54] A. Di Piazza, C. Müller, K. Z. Hatsagortsyan, and C. H. Keitel, Rev. Mod. Phys. **84**, 1177 (2012); arXiv:1111.3886 [hep-ph].
[55] V. B. Berestetskii, E. M. Lifshitz, and L. P. Pitaevskii, *Relativistic Quantum Theory* (Pergamon, Oxford, England, 1971).
[56] D. B. Blaschke, B. Kämpfer, S. M. Schmidt, A. D. Panferov, A. V. Prozorkevich, and S. A. Smolyansky, Phys. Rev. D. **88**, 045017 (2013); [arXiv:1301.1640 [physics.plasm-ph]].
[57] H. R. Reiss, Eur. Phys. J. D **55**, 365-374 (2009).
[58] C. Kohlfürst, H. Gies, and R. Alkofer, Phys. Rev. Lett. **112**, 050402 (2014); [arXiv:1310.7836 [hep-ph]].
[59] V. G. Bagrov, D. M. Gitman, and Sh. M. Shvartsman, Sov. Phys. JETP **41**, 191 (1975).
[60] D. M. Gitman, J. Phys. A **10**, 2007 (1977).
[61] J. P. Blaizot and G. Ripka, *Quantum Theory of Finite Systems* (MIT Press, Cambridge, MA, 1985).